

Coherent Electric-Field Control of Orbital State in a Neutral Nitrogen-Vacancy Center

Hodaka Kurokawa,^{1,*} Keidai Wakamatsu,² Shintaro Nakazato,² Toshiharu Makino,^{1,3} Hiromitsu Kato,^{1,3} Yuhei Sekiguchi,¹ and Hideo Kosaka^{1,2,†}

¹*Quantum Information Research Center, Institute of Advanced Sciences, Yokohama National University, 79-5 Tokiwadai, Hodogaya, Yokohama 240-8501, Japan*

²*Department of Physics, Graduate School of Engineering Science,*

Yokohama National University, 79-5 Tokiwadai, Hodogaya, Yokohama 240-8501, Japan

³*Advanced Power Electronics Research Center, National Institute of Advanced Industrial Science and Technology, 1-1-1 Umezono, Tsukuba, Ibaraki, 305-8568, Japan*

The coherent control of the orbital state is crucial for color centers in diamonds for realizing extremely low-power manipulation. Here, we propose the neutrally charged nitrogen-vacancy center, NV⁰, as an ideal system for orbital control through electric fields. We estimate electric susceptibility in the ground state of NV⁰ to be comparable to that in the excited state of NV⁻. Also, we demonstrate coherent control of the orbital states of NV⁰. The required power for orbital control is three orders of magnitude smaller than that for spin control, highlighting the potential for interfacing a superconducting qubit operated in a dilution refrigerator.

Diamond color centers are attracting broad attention because of their potential applications in quantum communication [1–3], quantum computation [4, 5], and quantum sensing [6, 7]. The spin degree of freedom is primarily utilized as a quantum bit, thanks to its long coherence time of over one second [8–10], and excellent controllability [11, 12]. On the other hand, control over the orbital degree of freedom is also crucial for some applications such as frequency tuning of the zero-phonon line photons and extremely low-power control of the electron states. The ability to tune the zero-phonon line frequency through electric fields or strain is essential for generating entanglement between remote color centers [1, 13, 14]. Moreover, the coupling of electric fields or strain with the orbital degree of freedom is more stronger compared to the magnetic field’s coupling with the spin [15–17], enabling highly efficient control of the electron state. With strong spin-orbit coupling, efficient spin-state control via strain has been achieved in color centers [18], which is particularly advantageous for operation in a dilution refrigerator. Nevertheless, directly achieving coherent control over the orbital state remains challenging for representative color centers due to the short lifetime of the optically excited state of NV⁻ (~ 10 ns) [19] and large ground-state splitting of group-IV color centers [20].

Here, we propose the neutrally charged nitrogen-vacancy center, NV⁰ [21–28], as an ideal system for orbital state control through electric fields. The ground-state spin-orbit splitting of NV⁰ is approximately 10 GHz [25, 26], enabling direct microwave access. Additionally, the ground state of NV⁰ exhibits an orbital relaxation time of several hundreds of nanoseconds [26], which is more than one order of magnitude longer than that of the excited state of NV⁻. Furthermore, the energy level

structure of the ground state in NV⁰ is similar to that of group-IV color centers. Therefore, NV⁰ can serve as an ideal system for understanding the properties of the orbital state and conducting proof-of-principle experiments relevant to group-IV color centers. In this paper, we investigate the electric susceptibility of NV⁰ and demonstrate coherent control over its orbital state. The highly efficient control opens up possibilities for future applications, such as a quantum interface communicating with a superconducting quantum bit in a dilution refrigerator [29, 30].

RESULTS

Characterization of NV⁰

Under a zero-magnetic field, the ground-state Hamiltonian, H , of NV⁰ in $|\pm\rangle_o$ basis can be modeled as [25, 26]

$$H^{(\pm)}/h = 2\lambda\hat{L}_z\hat{S}_z + \epsilon_{\perp}(\hat{L}_+ + \hat{L}_-), \quad (1)$$

where h is the Plank’s constant, λ is the spin-orbit interaction parameter, $\hat{L}_z = \sigma_z$, $\hat{L}_{\pm} = |\pm\rangle_o \langle \mp|_o$ are the orbital operator in $|\pm\rangle_o = \mp 1/\sqrt{2}(|e_x\rangle_o \pm i|e_y\rangle_o)$ basis, $|e_x\rangle_o$ and $|e_y\rangle_o$ are the strain eigenstates, $S_z = (1/2)\sigma_z$ is the spin operator for the 1/2 spin, and ϵ_{\perp} is the perpendicular strain parameter. Here, the subscripts o (s) denote the orbital (spin) degree of freedom. Figure 1 (a) shows the energy level of NV⁰. The ground-state splitting comes from the spin-orbit coupling, λ , and the strain, ϵ_{\perp} , as $2\sqrt{\lambda^2 + \epsilon_{\perp}^2}$. Under the strain, the eigenstates change from $|\pm\rangle_o$ to $|+\prime\rangle_o = \alpha|+\rangle_o + \beta|-\rangle_o$ and $|-\prime\rangle_o = -\beta|+\rangle_o + \alpha|-\rangle_o$ with $\alpha^2 + \beta^2 = 1$. Figure 1 (b) shows the electrical circuit directly formed on a diamond. The low (< 1 MHz) and high (~ 10 GHz) frequency electric fields are applied to nitrogen-vacancies using the upper electrodes. The color map of photoluminescence (PL)

* E-mail: kurokawa-hodaka-hm@ynu.ac.jp

† E-mail: kosaka-hideo-yp@ynu.ac.jp

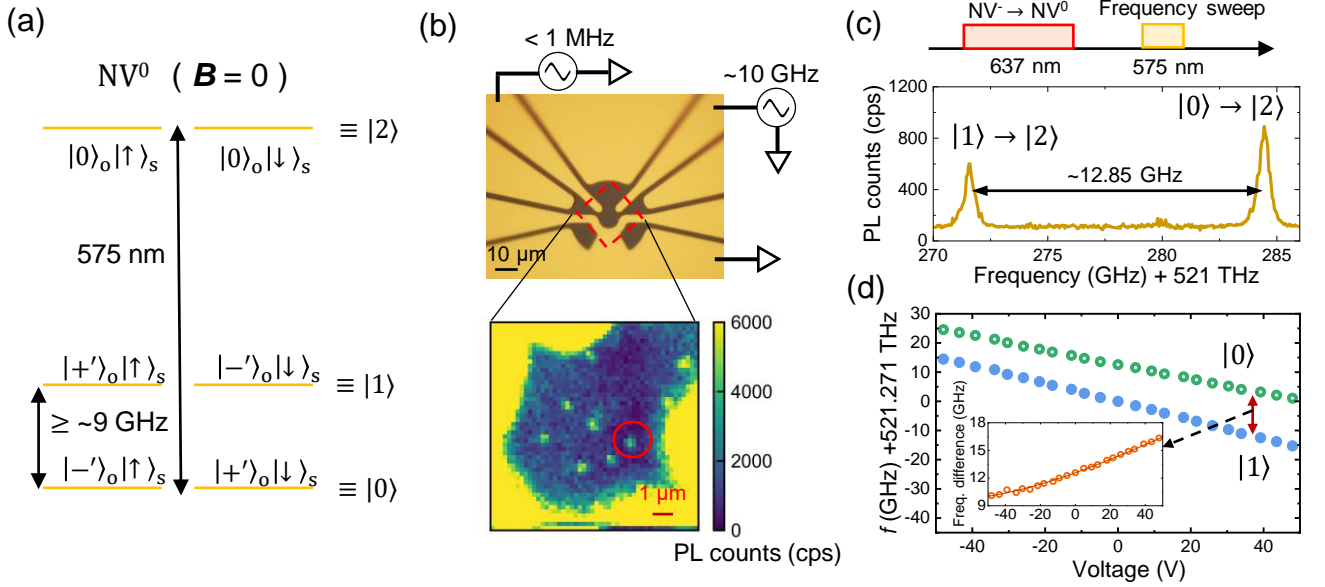


FIG. 1. The energy level structure of NV^0 , the device image, the photoluminescence excitation (PLE) spectrum, and the dc voltage dependence of the PLE spectrum. (a) Schematic of the energy level of NV^0 with some static strain under a zero magnetic field. ground state exhibits an energy splitting on the order of 10 GHz due to the combined effects of spin-orbit interaction and strain. The optical transition occurs at 575 nm. (b) An optical microscope image of the electrical circuit on the diamond used for experiments. The upper electrodes are used to apply low (< 1 MHz) or high (~ 10 GHz) electric fields. The color map shows the photoluminescence (PL) counts around the center of the circuit. The red-circled NV center is used for experiments. (c) The PLE spectrum of NV^0 and its measurement sequence. The 637 nm laser resonant to the zero-phonon line of NV^- is used to initialize the charge state to NV^0 . The 575 nm laser is used to observe the transition. (d) The PLE spectrum shifts as a function of dc voltage. Green and blue circles corresponds to the lower ($|0\rangle$) and upper ($|1\rangle$) branches, respectively. The inset shows the difference of the PLE frequencies between upper ($|0\rangle$) and lower ($|1\rangle$) branches. The horizontal axis is the same as the main graph.

counts around the center of the circuit is also shown. Figure 1 (c) shows the photoluminescence excitation (PLE) spectrum with the experimental sequence. A 637 nm red laser resonant to zero-phonon line (ZPL) of NV^- is used to convert NV^- to NV^0 . Frequencies of a 575 nm yellow laser are swept to search ZPL of NV^0 . Two transition lines are observed, indicating that the ground-state splitting is 12.85 GHz.

Since all the experiments are performed under an ambient magnetic field, the transitions from $|+\rangle_o|\uparrow\rangle_s$ and $|-\rangle_o|\downarrow\rangle_s$ can not be distinguished. Also, $|-\rangle_o|\uparrow\rangle_s$ and $|+\rangle_o|\downarrow\rangle_s$ are indistinguishable. In the following, we write as $|-\rangle_o|\uparrow\rangle_s = |+\rangle_o|\downarrow\rangle_s \equiv |0\rangle$, $|+\rangle_o|\uparrow\rangle_s = |-\rangle_o|\downarrow\rangle_s \equiv |1\rangle$, and $|0\rangle_o|\uparrow\rangle_s = |0\rangle_o|\downarrow\rangle_s \equiv |2\rangle$ ignoring the spin degree of freedom. In other words, we treat the four-level system in the ground state as effective two-level systems with different spin states. Since the lifetime of the spin reaches several milliseconds even under laser irradiation [26], the assumption is held as long as the laser irradiation time is sufficiently short.

Next, we apply dc electric fields to estimate the parameters in eq. (1) and the electric susceptibility. The effects of both strain and dc electric fields in $|\pm\rangle_o|\uparrow\rangle_s$ basis can

be written as:

$$H^{(\pm)}/h = \lambda \hat{L}_z + d_{\parallel} E_z \hat{I} + (\epsilon_{\perp} + d_{\perp} E_{\perp})(\hat{L}_+ + \hat{L}_-) + d_{\perp} E'_{\perp}(-i\hat{L}_+ + i\hat{L}_-), \quad (2)$$

where d_{\parallel} (d_{\perp}) is the electric susceptibility parallel (perpendicular) to the NV axis, E_z is the electric fields parallel to the NV axis, E_{\perp} is the electric fields whose axis is same with the direction of ϵ_{\perp} , E'_{\perp} is the electric fields perpendicular to E_{\perp} and E_z . Here, we ignore the strain term which only contributes to the global shift of the energy (See Supplementary materials for details). The energy eigenvalues are $d_{\parallel} E_z \pm \sqrt{\lambda^2 + (\epsilon_{\perp} + E_{\perp})^2 + (d_{\perp} E'_{\perp})^2}$. Figure 1 (d) shows the PLE frequency shifts of both upper ($|1\rangle$) and lower ($|0\rangle$) branches as a function of the dc electric fields. With increasing the dc electric fields, the PLE frequencies of the two branches decrease almost linearly. With the application of ± 50 V, the PLE frequencies can be shifted up to ~ 30 GHz. The linear frequency shifts in both branches are caused by E_z . Using the electric fields distribution obtained from the finite element simulation, d_{\parallel} is estimated to be 1.08 MHz/(V cm^{-1}) (See Supplementary materials for details), which is similar to the reported value in the excited state of NV^- , 0.7 MHz/(V cm^{-1}) [17]. Addition-

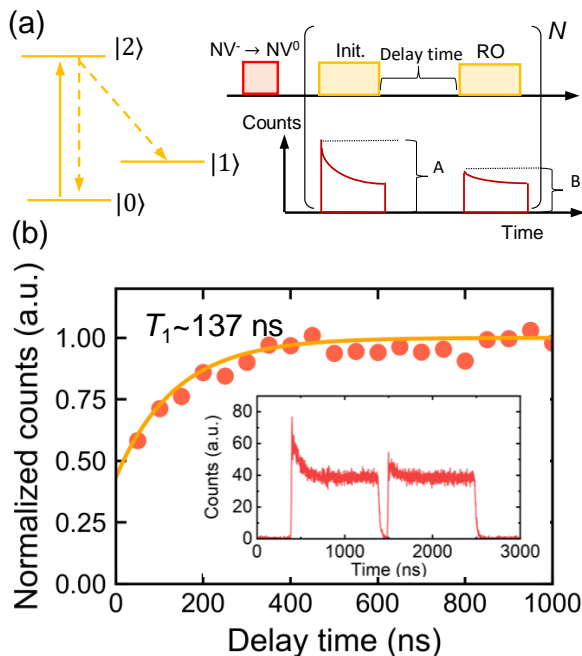


FIG. 2. Measurement of the orbital relaxation time of NV^0 . (a) Schematic of the experimental sequence for the measurement of the orbital relaxation time of NV^0 . After the charge initialization (Init.) using the 637 nm laser, the first 575 nm laser pulse initializes $|0\rangle$ to $|1\rangle$ and the population in $|0\rangle$ is read out (RO) by the second 575 nm pulse after some delay time. The peak counts, A and B , at each pulse are used to estimate the population in $|0\rangle$. The repetition times for each measurement, N , are 150 which is determined from the measurement of the decay of the PL counts as a function of the duration of the 575 nm laser irradiation. (b) The normalized counts, B/A , as a function of the delay time. The red dots are the experimental data and the orange curve is the result of the curve fit with the exponential function. The inset shows The time-resolved PL counts with 100 ns delay. The PL counts are smoothed using the Savitzky-Golay filter with 17 points before the calculation of the peak height. The background is subtracted using the data when the laser is absent.

ally, the frequency shifts due to E_{\perp} and E'_{\perp} can be seen clearly by subtracting the upper PLE frequencies from the lower PLE frequencies (The inset of Fig. 1 (d)). The frequency differences are fitted with the equation, $2\sqrt{\lambda^2 + (\epsilon_{\perp} + d_{\perp}E_{\perp})^2 + (d_{\perp}E'_{\perp})^2}$ with a fixed $\lambda = 4.80$ GHz [26]. The parameters are estimated to be $\epsilon_{\perp} = 4.06$ GHz and $d_{\perp} = 363$ kHz/(V cm $^{-1}$). Note that d_{\perp} is several times smaller than the value reported in Ref. [17] for the excited state of NV^{-} , 1.4 MHz/(V cm $^{-1}$).

The orbital relaxation of NV^0

The orbital relaxation time, T_1 , is important since it determines the limit of operation time. Figure 2 (a) shows the experimental sequence for the measurement of

T_1 . A 1- μ s long optical pulse resonant to the transition between $|0\rangle$ and $|2\rangle$ initializes NV^0 into $|1\rangle$ from thermal mixture of $|0\rangle$ and $|1\rangle$ (The inset of Fig. 2 (b)). The first peak height is proportional to the initial population in $|0\rangle$. The peak height in the second pulse is proportional to the population in $|0\rangle$ relaxed from $|1\rangle$. The ratio of the pulse heights in the first and second pulses is a measure of decay from $|1\rangle$, which are used to calculate T_1 . Figure 2 (b) shows the normalized pulse height as a function of the delay of the second pulse. T_1 is estimated to be ~ 137 ns at 5.5 K from the curve fit with $1 - a\exp(-t/T_1) + b$, where a and b are some constants. In Ref. [26], T_1 is a few times larger than ours. At 5.5 K, T_1 should be limited by thermal phonons. Further increase of T_1 is expected by decreasing temperature down to several tens of millikelvin.

Optically detected electrical resonance and the Rabi splitting

To investigate the electrical resonance frequency in the ground state of NV^0 , we employ the optically detected electrical resonance (ODER). Since we apply the driving electric fields resonant to the eigenfrequency determined by λ and ϵ_{\perp} , we treat the ac driving electric fields as a perturbation to the eigenstates of the strain, $|\pm'\rangle_o$. In the rotating frame of the driving ac electric fields, $H_d/h = f_d \hat{L}_z/2$, under the rotating wave approximation, Hamiltonian of NV^0 in $|\pm'\rangle_o$ basis can be written as:

$$H^{(\pm)}/h = \Delta \hat{L}_z + d_{\perp} E''_{\perp} (\hat{L}_+ + \hat{L}_-), \quad (3)$$

where f_d is the frequency of the driving electric fields, $\Delta = \sqrt{\lambda^2 + \epsilon_{\perp}^2} - f_d$ is the detuning, $E''_{\perp} = \sqrt{(\alpha^2 - \beta^2)E_x^2 + E_y^2}$ is the electric fields perpendicular to the NV axis, and E_x and E_y are the in-plane electric fields (See Supplementary materials for details). Here, \hat{L}_{\pm} are the rising (lowering) operators in $|\pm'\rangle_o$ basis. When $\Delta \sim 0$, the remained second term in eq. (3) contributes to the Rabi splitting and the Rabi oscillation, which will be discussed in the following.

Figure 3 (a) shows the experimental sequence. The microwave frequencies are swept around frequency resonant to the transition between $|0\rangle$ and $|1\rangle$, which is roughly estimated from the PLE measurement. At the same time, the readout laser is applied to measure the population in $|0\rangle$. A sufficiently long readout pulse increases the population in $|1\rangle$ through the optical pumping as shown in the inset of Fig. 2 (b). When the microwave frequency and the ground-state splitting are in resonance, the population in $|1\rangle$ is transferred to $|0\rangle$, resulting in the increase of PL counts. Figure 3 (b) shows the result of the ODER. The maximum of the spectrum is 12.84 GHz, which is in good agreement with the ground-state splitting obtained from the PLE measurement. The full width at half maximum (FWHM) is 130 MHz, which is due to the spectral diffusion in the ground and optically excited states.

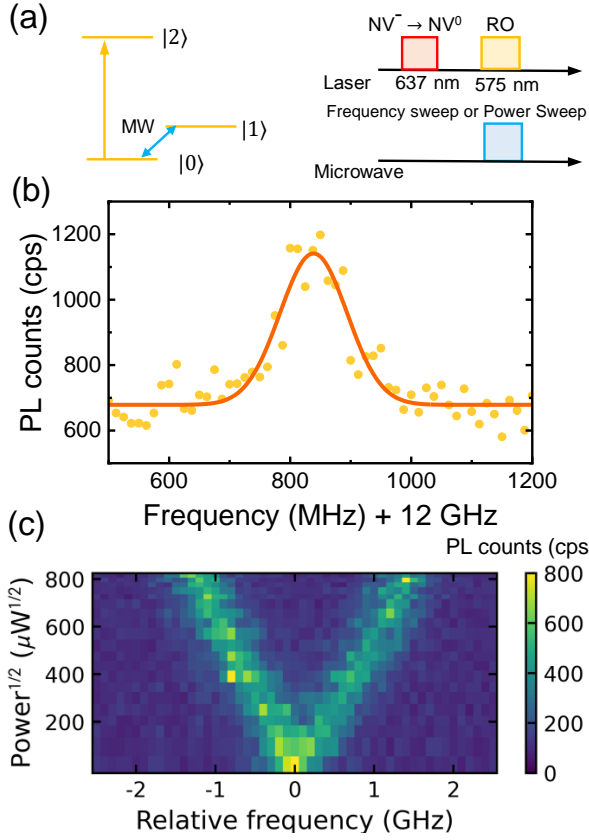


FIG. 3. The optically detected electrical resonance (ODER) and the Rabi splitting measurements. (a) Schematic of the experimental sequence for the measurements of ODER and the Rabi splitting. After the charge conversion by the 637 nm laser, the 575 nm laser resonant to the transition between $|0\rangle$ and $|2\rangle$ is applied simultaneously with microwave application. Frequencies of the 575 nm laser are swept for the ODER measurement. The power of the microwave is swept for the measurement of the Rabi splitting. (b) The ODER spectrum of NV^0 . The orange dots are the data and the red curve is the Gaussian fit. (c) The Rabi splitting as a function of the square root of the power of the applied microwave electric fields.

Using the resonance frequency (12.84 GHz) obtained from the ODER measurement, we investigate the microwave power dependence of the Rabi splitting by increasing the microwave power. Figure 3 (c) shows the color map of the PL counts as functions of the relative frequency and the square root of the microwave power. The maximum Rabi splitting is 2.6 GHz at $824 \mu W^{1/2}$. The power dependence of the Rabi splitting directly corresponds to the power dependence of the Rabi frequency, which is estimated to be $3.37 \text{ MHz}/\mu W^{1/2}$ from the fitting. Also, the electric susceptibility are estimated to be $\epsilon_{\perp}^{\text{ac}} = 961 \text{ kHz}/(\text{V cm}^{-1})$ (See Supplementary materials for details). $\epsilon_{\perp}^{\text{ac}}$ is larger than that obtained using dc electric fields, $363 \text{ kHz}/(\text{V cm}^{-1})$. The difference can be attributed to the electric field screening in the dc mea-

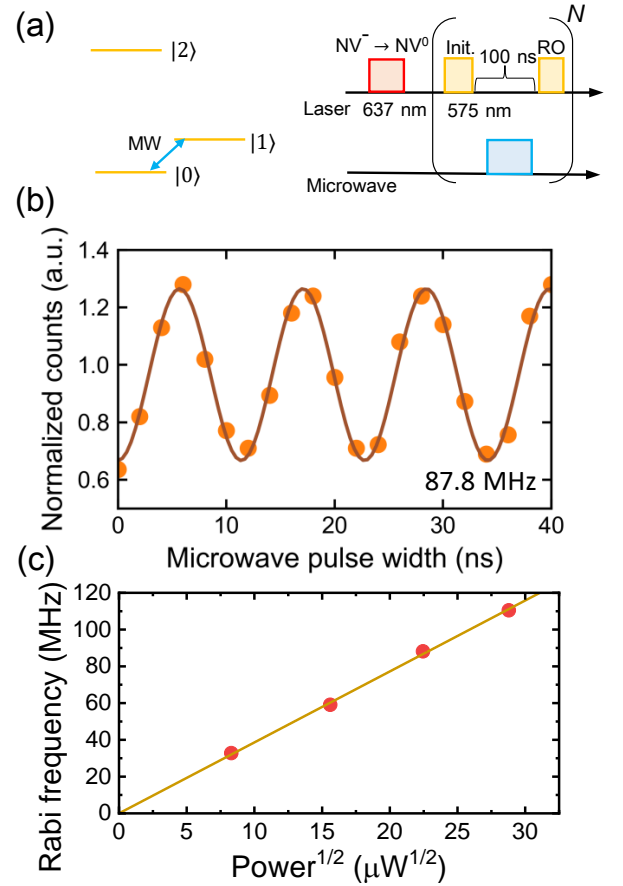


FIG. 4. The Rabi oscillation and the microwave power dependence of the Rabi frequency. (a) Schematic of the experimental sequence for the Rabi oscillation. The microwave pulse is applied between the first (initialization) and second (readout) laser pulses. The microwave frequency is set to the resonance frequency obtained from the ODER. The repetition times, N , are 100. (b) Normalized counts as a function of the microwave pulse width. The orange dots are the data and the brown curve is the cosinusoidal fit. The Rabi frequency is 87.8 MHz. (c) The Rabi frequency as a function of the square root of the input power. The slope is $3.86 \text{ MHz}/\mu W^{1/2}$.

surement, which decreased the effective electric fields at the NV center [17]. The value of $\epsilon_{\perp}^{\text{ac}}$ is in good agreement with that of the optically excited state of NV^- , $1.4 \text{ MHz}/(\text{V cm}^{-1})$ [17].

The Rabi oscillation and the Ramsey interference

Using the resonance frequency obtained from the ODER measurement, the Rabi oscillations between $|0\rangle$ and $|1\rangle$ are observed. Figure 4 (a) shows the experimental sequence for the measurement. The microwave pulse is applied between the two laser pulses. Figure 4 (b) shows the Rabi oscillation at the input microwave power of $828 \mu W$. The Rabi frequency is 87.8 MHz. Compared

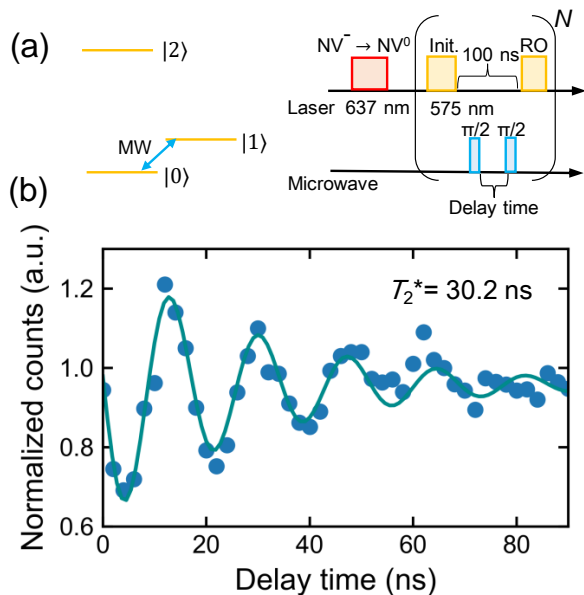


FIG. 5. The Ramsey interference. (a) Schematic of the experimental sequence for the Ramsey interference. The two microwave pulses are applied between the first (initialization) and second (readout) laser pulses. The microwave width for $\pi/2$ pulse is determined to be 4.6 ns from the measurement of the Rabi oscillation. The repetition times, N , are 100. (b) The normalized counts as a function of the delay time of the microwave pulse (free precession time). The blue dots are the data and the blue curve is the fit with the function, $A\sin(\omega t + \phi)\exp(-t/T_2^*) + B$, where A , B , and ϕ are some constants, ω is the angular frequency, and T_2^* is the orbital coherence time. T_2^* is 30.2 ns.

to the power required to drive the spin of NV^- at a similar distance from the electrode (several μm), the required power is three orders of magnitude smaller. Figure 4 (c) shows the Rabi frequency as a function of the square root of the microwave power. The Rabi frequency increases linearly with the square root of the microwave power. The slope is $3.86 \text{ MHz}/\mu\text{W}^{1/2}$, which is in good agreement with the value obtained from the measurement of the Rabi splitting, $3.37 \text{ MHz}/\mu\text{W}^{1/2}$.

We also investigate the coherence time, T_2^* , of the orbital state using the Ramsey interference. Figure 5 (a) shows the experimental sequence. The two microwave $\pi/2$ pulses are applied between the initialize and readout laser pulses. Figure 5 (b) shows the Ramsey interference with some detuning as a function of free precession time. From the curve fit, the detuning is 58 MHz and T_2^* is 30.2 ns. Origins of the decoherence are attributed to the surrounding nuclear spins [31, 32], the spectral diffusion [33] in the ground state, and thermal phonons resonant with the orbital transition as proposed for SiV [34]. The value of T_2^* is similar to the spin coherence time of SiV at around 5 K (30-50 ns) [18, 35, 36]. Thus, a further increase of T_2^* is expected by decreasing the temperature

as SiV and the dynamical decoupling.

DISCUSSION

In conclusion, we have measured the electric susceptibility of NV^0 in the ground state, which is comparable to that in the excited state of NV^- . Also, we have also succeeded in coherent control over the orbital state of NV^0 using electric fields. The required power for the Rabi oscillation is hundreds of microwatts, which is three orders of magnitude smaller than that required for the spin control using magnetic fields. The highly efficient control is advantageous especially for the operation in a dilution refrigerator, opening up the possibility for interfacing a superconducting qubit and a color center via electric fields. If we can integrate a high impedance superconducting microwave resonator with zero-point voltage fluctuation tens of microvolts [37, 38], the single-photon coupling is expected to be tens of kilohertz, enabling the microwave control using several hundred photons.

Moreover, the control using phonons is promising. Since the mode volume of the phononic resonator can be designed to be several orders of magnitude smaller than that of typical microwave resonators [29, 39], the single-phonon coupling can exceed 1 MHz, enabling the realization of the strong coupling between a single phonon and NV^0 .

Although the measured T_1 has been 137 ns at 5.5 K, it is expected to extend to microseconds in the environment of a dilution refrigerator due to a decrease in thermal phonons. If it reaches several microseconds, it is sufficient to use for an interface between a superconducting quantum bit [30], which is proposed for the silicon-vacancy center [29]. Despite a lot of challenges posed by the spectral diffusion, integration of a microwave resonator, and operation in a dilution refrigerator, our study demonstrates a promising path toward hybrid quantum systems.

METHODS

Sample fabrication

We use [100]-cut, electronic grade single-crystal diamond samples synthesized by chemical vapor deposition (CVD) (Element Six). Before the fabrication of the electrode, the diamond substrate is kept in a mixture of H_2SO_4 and HNO_3 at 200°C for 60 min to remove any surface contamination and terminate the surface with oxygen. Then, Au (500 nm) / Ti (10nm) electrodes are formed on the substrate by using photolithography processes.

Low temperature confocal microscopy

All experiments are performed in a closed-cycle optical cryostat (Cryostation s50, Montana Instruments) at 5.5 K under an ambient magnetic field. A copper sample holder is mounted on XYZ piezoelectric nanopositioners (ANPx101×2, ANPz101) using a thermal link. The diamond sample is fixed onto a homemade printed circuit board (PCB) using aluminum tapes. The electrodes on the diamond are connected to the PCB via gold wire bonds. The PCB is attached to the sample holder with screws.

Optical excitation and collection are done using a home-built confocal microscope. An objective lens (LM-PLFLN100X, Olympus), whose numerical aperture is 0.8, is scanned over the sample using a XYZ piezoelectric nanopositioner (P-517.3CD, Physik Instrumente).

A 515 nm green laser (Cobolt, Hubner Photonics) is used for off-resonant excitation to search nitrogen-vacancy centers. A 575 nm yellow laser (DL-SHG pro, Toptica Photonics) is used to resonantly excite NV^0 for initialization and readout. Typically, a 1 μ s pulse is used and the power is 1 μ W. A 637 nm red laser (DL pro, Toptica Photonics) is used to resonantly excite NV^- to convert the negatively charged state to the neutrally charged state. The pulse width for the charge initialization is 100 μ s and the power is 200 μ W. Each laser joins to the main optical path using dichroic mirrors (FF552-Di02-25x36: 515 nm, FF605-Di02-25x36: 575 nm, FF649-Di01-25x36: 637 nm, Semrock) after purified through bandpass filters (FF02-520/28-25: 515 nm, FF03-575/25-25: 575 nm, FF01-637/7-25: 637 nm, Semrock).

The power of 515 nm laser is controlled by setting the internal output power. The powers of 575 nm and 637 nm lasers are controlled using variable fiber optic attenuators (V450PA: 575 nm, V600PA: 637 nm, Thorlabs). The pulse duration of 515 nm laser is directly set by the signal sent from a field programmable gate array (FPGA). The pulse durations of 575 nm and 637 nm laser are gated using acousto-optic modulators (SFO4903-S-M200 0.4C2C-3-F2P-01: 575 nm, SFO3916-S-M200-0.4C2E-3-F2P-02: 637 nm, Gooch and Housego) controlled by the FPGA (PXIe-7820R, National Instruments).

The phonon sideband of NV^0 and NV^- is collected and measured using a single-photon counter (SPCM-AQRH-14-FC, Excelitas). For the time-resolved photolumines-

cence measurements, the signal from the single-photon counter is sent to a time-resolved single-photon counter (PicoHarp300, PicoQuant). The time-bin is set to be 512 ps.

DC and ac electronics for measurements

The dc voltages are generated using an arbitrary waveform generator (M3202A, Keysight). The voltages are amplified using amplifiers (EVAL-ADHV4702-1CPZ, Analog Devices). The microwave voltages up to 16 GHz (> 25 GHz for a single channel) are generated using another arbitrary waveform generator (M8195A, Keysight). The microwave voltages are amplified using an amplifier (ZVE-3W-183+, Mini Circuits). The microwave power at the sample is estimated using a network analyzer (P9373A, Keysight). The loss inside the cryostat is estimated from the reflection coefficient, S_{11} , inside the cryostat. Assuming equal energy loss on the way to the sample and on the way back, half of S_{11} corresponds to the loss between the input port and the sample.

ACKNOWLEDGEMENTS

This work was supported by a Japan Science and Technology Agency (JST) Moonshot R&D grant (JPMJMS2062) and by a JST CREST grant (JPMJCR1773). We also acknowledge the Ministry of Internal Affairs and Communications (MIC) for funding, research and development for construction of a global quantum cryptography network (JPMI00316) and the Japan Society for the Promotion of Science (JSPS) Grants-in-Aid for Scientific Research (20H05661, 20K20441).

AUTHORSHIP CONTRIBUTION

H. Kurokawa and Y. S. designed the experiments. H. Kurokawa wrote the manuscript. K. W. and S. N performed the experiments. T. M and H. Kato fabricated the electrical circuit. H. Kosaka supervised the project.

-
- [1] H. Bernien, B. Hensen, W. Pfaff, G. Koolstra, M. S. Blok, L. Robledo, T. H. Taminiau, M. Markham, D. J. Twitchen, L. Childress, and R. Hanson, *Nature* **497**, 86 (2013).
 - [2] M. Pompili, S. L. N. Hermans, S. Baier, H. K. C. Beukers, P. C. Humphreys, R. N. Schouten, R. F. L. Vermeulen, M. J. Tiggelman, L. dos Santos Martins, B. Dirkse, S. Wehner, and R. Hanson, *Science* **372**, 259 (2021).
 - [3] M. K. Bhaskar, R. Riedinger, B. Machielse, D. S. Levonian, C. T. Nguyen, E. N. Knall, H. Park, D. Englund, M. Lončar, D. D. Sukachev, and M. D. Lukin, *Nature* **580**, 60 (2020).
 - [4] K. Nemoto, M. Trupke, S. J. Devitt, A. M. Stephens, B. Scharfenberger, K. Buczak, T. Nöbauer, M. S. Everitt, J. Schmiedmayer, and W. J. Munro, *Physical Review X* **4**, 031022 (2014).

- [5] M. H. Abobeih, J. Randall, C. E. Bradley, H. P. Bartling, M. A. Bakker, M. J. Degen, M. Markham, D. J. Twitchen, and T. H. Taminiau, *Nature* **576**, 411 (2019).
- [6] F. Dolde, H. Fedder, M. W. Doherty, T. Nöbauer, F. Rempp, G. Balasubramanian, T. Wolf, F. Reinhard, L. C. L. Hollenberg, F. Jelezko, and J. Wrachtrup, *Nature Physics* **7**, 459 (2011).
- [7] C. L. Degen, F. Reinhard, and P. Cappellaro, *Reviews of Modern Physics* **89**, 035002 (2017).
- [8] G. Balasubramanian, P. Neumann, D. Twitchen, M. Markham, R. Kolesov, N. Mizuochi, J. Isoya, J. Achard, J. Beck, J. Tissler, V. Jacques, P. R. Hemmer, F. Jelezko, and J. Wrachtrup, *Nature Materials* **8**, 383 (2009).
- [9] N. Bar-Gill, L. M. Pham, A. Jarmola, D. Budker, and R. L. Walsworth, *Nature Communications* **4**, 1743 (2013).
- [10] M. H. Abobeih, J. Cramer, M. A. Bakker, N. Kalb, M. Markham, D. J. Twitchen, and T. H. Taminiau, *Nature Communications* **9**, 2552 (2018).
- [11] M. H. Abobeih, Y. Wang, J. Randall, S. J. H. Loenen, C. E. Bradley, M. Markham, D. J. Twitchen, B. M. Terhal, and T. H. Taminiau, *Nature* **606**, 884 (2022).
- [12] C. T. Nguyen, D. D. Sukachev, M. K. Bhaskar, B. Machielse, D. S. Levonian, E. N. Knall, P. Stroganov, R. Riedinger, H. Park, M. Lončar, and M. D. Lukin, *Physical Review Letters* **123**, 183602 (2019).
- [13] P. Tamarat, N. B. Manson, J. P. Harrison, R. L. McMurtre, A. Nizovtsev, C. Santori, R. G. Beausoleil, P. Neumann, T. Gaebel, F. Jelezko, P. Hemmer, and J. Wrachtrup, *New Journal of Physics* **10**, 045004 (2008).
- [14] J. R. Maze, A. Gali, E. Togan, Y. Chu, A. Trifonov, E. Kaxiras, and M. D. Lukin, *New Journal of Physics* **13**, 025025 (2011).
- [15] S. Meesala, Y.-I. Sohn, B. Pingault, L. Shao, H. A. Atikian, J. Holzgrafe, M. Gündogan, C. Stavrakas, A. Sipahigil, C. Chia, R. Evans, M. J. Burek, M. Zhang, L. Wu, J. L. Pacheco, J. Abraham, E. Bielejec, M. D. Lukin, M. Atatüre, and M. Lončar, *Physical Review B* **97**, 205444 (2018).
- [16] H. Y. Chen, E. R. MacQuarrie, and G. D. Fuchs, *Physical Review Letters* **120**, 167401 (2018).
- [17] M. Block, B. Kobrin, A. Jarmola, S. Hsieh, C. Zu, N. L. Figueroa, V. M. Acosta, J. Minguzzi, J. R. Maze, D. Budker, and N. Y. Yao, *Physical Review Applied* **16**, 024024 (2021).
- [18] S. Maity, L. Shao, S. Bogdanović, S. Meesala, Y.-I. Sohn, N. Sinclair, B. Pingault, M. Chalupnik, C. Chia, L. Zheng, K. Lai, and M. Lončar, *Nature Communications* **11**, 193 (2020).
- [19] A. Batalov, C. Zierl, T. Gaebel, P. Neumann, I.-Y. Chan, G. Balasubramanian, P. R. Hemmer, F. Jelezko, and J. Wrachtrup, *Physical Review Letters* **100**, 077401 (2008).
- [20] G. Wolfowicz, F. J. Heremans, C. P. Anderson, S. Kanai, H. Seo, A. Gali, G. Galli, and D. D. Awschalom, *Nature Reviews Materials* **6**, 906 (2020).
- [21] N. B. Manson and J. P. Harrison, *Diamond and Related Materials* **14**, 1705 (2005).
- [22] M. V. Hauf, B. Grotz, B. Naydenov, M. Dankerl, S. Pezzagna, J. Meijer, F. Jelezko, J. Wrachtrup, M. Stutzmann, F. Reinhard, and J. A. Garrido, *Physical Review B* **83**, 081304 (2011).
- [23] B. Grotz, M. V. Hauf, M. Dankerl, B. Naydenov, S. Pezzagna, J. Meijer, F. Jelezko, J. Wrachtrup, M. Stutzmann, F. Reinhard, and J. A. Garrido, *Nature Communications* **3**, 729 (2012).
- [24] Y. Doi, T. Makino, H. Kato, D. Takeuchi, M. Ogura, H. Okushi, H. Morishita, T. Tashima, S. Miwa, S. Yamasaki, P. Neumann, J. Wrachtrup, Y. Suzuki, and N. Mizuochi, *Physical Review X* **4**, 011057 (2014).
- [25] M. S. Barson, E. Krausz, N. B. Manson, and M. W. Doherty, *Nanophotonics* **8**, 1985 (2019).
- [26] S. Baier, C. E. Bradley, T. Middelburg, V. V. Dobrovitski, T. H. Taminiau, and R. Hanson, *Physical Review Letters* **125**, 193601 (2020).
- [27] Q. Zhang, Y. Guo, W. Ji, M. Wang, J. Yin, F. Kong, Y. Lin, C. Yin, F. Shi, Y. Wang, and J. Du, *Nature Communications* **12**, 1529 (2021).
- [28] N. Aslam, G. Waldherr, P. Neumann, F. Jelezko, and J. Wrachtrup, *New Journal of Physics* **15**, 013064 (2013).
- [29] T. Neuman, M. Eichenfield, M. E. Trusheim, L. Hackett, P. Narang, and D. Englund, *npj Quantum Information* **7**, 121 (2021).
- [30] H. Kurokawa, M. Yamamoto, Y. Sekiguchi, and H. Kosaka, *Physical Review Applied* **18**, 064039 (2022).
- [31] J. N. Becker, B. Pingault, D. Groß, M. Gündogan, N. Kukharchyk, M. Markham, A. Edmonds, M. Atatüre, P. Bushev, and C. Becher, *Physical Review Letters* **120**, 053603 (2018).
- [32] C. T. Nguyen, D. D. Sukachev, M. K. Bhaskar, B. Machielse, D. S. Levonian, E. N. Knall, P. Stroganov, C. Chia, M. J. Burek, R. Riedinger, H. Park, M. Lončar, and M. D. Lukin, *Physical Review B* **100**, 165428 (2019).
- [33] L. Robledo, H. Bernien, I. van Weperen, and R. Hanson, *Physical Review Letters* **105**, 177403 (2010).
- [34] K. D. Jahnke, A. Sipahigil, J. M. Binder, M. W. Doherty, M. Metsch, L. J. Rogers, N. B. Manson, M. D. Lukin, and F. Jelezko, *New Journal of Physics* **17**, 043011 (2015).
- [35] L. J. Rogers, K. D. Jahnke, M. H. Metsch, A. Sipahigil, J. M. Binder, T. Teraji, H. Sumiya, J. Isoya, M. D. Lukin, P. Hemmer, and F. Jelezko, *Physical Review Letters* **113**, 263602 (2014).
- [36] B. Pingault, J. N. Becker, C. H. H. Schulte, C. Arend, C. Hepp, T. Godde, A. I. Tartakovskii, M. Markham, C. Becher, and M. Atatüre, *Physical Review Letters* **113**, 263601 (2014).
- [37] N. Samkharadze, A. Bruno, P. Scarlino, G. Zheng, D. P. DiVincenzo, L. DiCarlo, and L. M. K. Vandersypen, *Physical Review Applied* **5**, 044004 (2016).
- [38] D. Niepce, J. Burnett, and J. Bylander, *Physical Review Applied* **11**, 044014 (2019).
- [39] B. Kim, H. Kurokawa, H. Kosaka, and M. Nomura, *arXiv:2305.08306* .

Supplementary Material for : Coherent Electric Field Orbital Control of Neutral Nitrogen-Vacancy Center

Hodaka Kurokawa,^{1,*} Keidai Wakamatsu,² Shintaro Nakazato,² Toshiharu
Makino,³ Hiromitsu Kato,³ Yuhei Sekiguchi,¹ and Hideo Kosaka^{1,2,†}

¹*Quantum Information Research Center,
Institute of Advanced Sciences, Yokohama National University,
79-5 Tokiwadai, Hodogaya, Yokohama 240-8501, Japan*

²*Department of Physics, Graduate School of Engineering Science,
Yokohama National University, 79-5 Tokiwadai,
Hodogaya, Yokohama 240-8501, Japan*

³*Advanced Power Electronics Research Center,
National Institute of Advanced Industrial Science and Technology,
1-1-1 Umezono, Tsukuba, Ibaraki, 305-8568, Japan*

I. THE HAMILTONIAN OF NV⁰

When magnetic fields and strain are zero, the Hamiltonian of NV⁰ can be written in basis $|\pm\rangle_o = \mp(|e_x\rangle_o \pm i|e_y\rangle_o)$ as follows:

$$H_0^{(\pm)}/h = 2\lambda\hat{L}_z\hat{S}_z, \quad (1)$$

where h is the Plank's constant, λ is the spin-orbit interaction parameter, $\hat{L}_z = \sigma_z$, $\hat{L}_\pm = |\pm\rangle_o \langle \mp|_o$ are the orbital operator in $|\pm\rangle_o = \mp 1/\sqrt{2}(|e_x\rangle_o \pm i|e_y\rangle_o)$ basis, $|e_x\rangle_o$ and $|e_y\rangle_o$ are the strain eigenstates, $S_z = (1/2)\sigma_z$ is the spin operator for the 1/2 spin. Since NV⁰ has the same wave function symmetry as NV⁻, we consider that the effects of the strain and the electric fields on $|e_{x,y}\rangle_o$ are similar to that in the excited state of NV⁻ [1]. Thus, we apply the discussion about the excited state of NV⁻ in Ref. [1] for NV⁰ in the following. In the $|e_{x,y}\rangle_o$ basis, the strain and electric fields Hamiltonian can be written as:

$$H_{\text{strain}}^{(e_{x,y})}/h = \epsilon_{A_1}\hat{I} + \epsilon_{E_1}\hat{\sigma}_z - \epsilon_{E_2}\hat{\sigma}_x, \quad (2)$$

$$H_{\text{electric}}^{(e_{x,y})}/h = d_{\parallel}E_z\hat{I} + d_{\perp}E_x\hat{\sigma}_z - d_{\perp}E_y\hat{\sigma}_x, \quad (3)$$

where ϵ_{A_1} , ϵ_{E_1} , and ϵ_{E_2} represent the strain in the energy dimensions with symmetric indices. d_{\perp} denotes the in-plane electric susceptibility, while d_{\parallel} represents the electric susceptibility along the NV axis. In $|\pm\rangle_o$ basis,

$$H_{\text{strain}}^{(\pm)}/h = \epsilon_{A_1}\hat{I} - \epsilon_{E_1}(\hat{L}_+ + \hat{L}_-) - \epsilon_{E_2}(-i\hat{L}_+ + i\hat{L}_-), \quad (4)$$

$$H_{\text{electric}}^{(\pm)}/h = d_{\parallel}E_z\hat{I} - d_{\perp}E_x(\hat{L}_+ + \hat{L}_-) - d_{\perp}E_y(-i\hat{L}_+ + i\hat{L}_-). \quad (5)$$

In order to simplify the analysis, we will consider only the subspace of spin in the state $|\uparrow\rangle_s$, as strain and electric fields do not directly affect the spin.

A. The strain and the dc electric fields

First, consider the state where only strain is present in the system. For the strain Hamiltonian, we can redefine the axis of rotation for simplicity and express it as follows:

$$H_{\text{strain}}^{(\pm)}/h = \epsilon_{1A}\hat{I} + \epsilon_{\perp}(\hat{L}_+ + \hat{L}_-). \quad (6)$$

* E-mail: kurokawa-hodaka-hm@ynu.ac.jp

† E-mail: kosaka-hideo-yp@ynu.ac.jp

Regarding the electric fields, since they may not necessarily align with the same direction as the strain, we can rewrite it as:

$$H_{\text{electric}}^{(\pm)}/h = d_{\parallel}E_z\hat{I} + d_{\perp}E_{\perp}(\hat{L}_+ + \hat{L}_-) + d_{\perp}E'_{\perp}(-i\hat{L}_+ + i\hat{L}_-), \quad (7)$$

where E_{\perp} is the electric fields with the same direction as ϵ_{\perp} and E'_{\perp} is the electric fields perpendicular to E_z and E'_{\perp} . To diagonalize these equations, $H_0 + H_{\text{strain}} + H_{\text{electric}}$, we obtain the energy eigenvalues as:

$$E_{\pm} = (\epsilon_{1A} + d_{\parallel}E_z) \pm \sqrt{\lambda^2 + (\epsilon_{\perp} + d_{\perp}E_{\perp})^2 + (d_{\perp}E'_{\perp})^2}. \quad (8)$$

The corresponding eigenvectors, without normalization coefficients, can be written as:

$$|+\rangle_{\circ} = \frac{\lambda + \sqrt{\lambda^2 + (\epsilon_{\perp} + d_{\perp}E_{\perp})^2 + (d_{\perp}E'_{\perp})^2}}{\epsilon_{\perp} + d_{\perp}E_{\perp} + id_{\perp}E'_{\perp}} |+\rangle_{\circ} + |-\rangle_{\circ}, \quad (9)$$

$$|-\rangle_{\circ} = \frac{\lambda - \sqrt{\lambda^2 + (\epsilon_{\perp} + d_{\perp}E_{\perp})^2 + (d_{\perp}E'_{\perp})^2}}{\epsilon_{\perp} + d_{\perp}E_{\perp} + id_{\perp}E'_{\perp}} |+\rangle_{\circ} + |-\rangle_{\circ}. \quad (10)$$

B. The strain and the ac electric fields

The ac electric fields are applied in such a way that it resonates with the eigenstates of the strain, $|\pm\rangle_{\circ}$ ($\mathbf{E} = 0$). Therefore, the ac electric fields are treated as a perturbation to the eigenstates of the strain.

The effects of the electric fields in the basis of $|\pm\rangle_{\circ}$ with normalized eigenvectors $|+\rangle_{\circ} = \alpha|+\rangle_{\circ} + \beta|-\rangle_{\circ}$ and $|-\rangle_{\circ} = -\beta|+\rangle_{\circ} + \alpha|-\rangle_{\circ}$ can be expressed as:

$$H_{\text{electric}}^{(\pm)}/h = d_{\parallel}E_z\hat{I} - d_{\perp}E_x[(\alpha^2 - \beta^2)(\hat{L}_+ + \hat{L}_-) + 2\alpha\beta\hat{\sigma}_z] - d_{\perp}E_y(-i\hat{L}_+ + i\hat{L}_-), \quad (11)$$

where \hat{L}_{\pm} are the rising (lowering) operators in $|\pm\rangle_{\circ}$ basis. Here is the equation with the redefined axis after introducing $E'_{\perp} = \sqrt{(\alpha^2 - \beta^2)^2 E_x^2 + E_y^2}$:

$$H_{\text{electric}}^{(\pm)}/h = d_{\parallel}E_z\hat{I} + d_{\perp}E'_{\perp}(\hat{L}_+ + \hat{L}_-) + 2d_{\perp}E_x\alpha\beta\hat{L}_z \quad (12)$$

Then, we move to the rotating frame with $H_{\text{rot}}/h = f_d\hat{L}_z/2$ from the system Hamiltonian, $\sqrt{\lambda^2 + \epsilon_{\perp}^2}\hat{L}_z + H_{\text{electric}}^{(\pm)}/h$. Under the rotating wave approximation, the equation result in

$$H_{\text{electric}}^{(\pm)}/h = \Delta\hat{\sigma}_z + d_{\perp}E'_{\perp}(\hat{L}_+ + \hat{L}_-). \quad (13)$$

Thus, when $\Delta = \sqrt{\lambda^2 + \epsilon_{\perp}^2} - f_d = 0$, we can observe the Rabi oscillation between the orbital states.

II. THE ESTIMATION OF THE APPLIED ELECTRIC FIELD

The electric fields versus the applied voltage are estimated from a simulation of the electric field distribution using the finite element method (FEM) (COMSOL Multiphysics, COMSOL). The electric fields at the NV center are estimated to be $(E_X, E_Y, E_Z) = (12497.6 \text{ V/m}, -26122.3 \text{ V/m}, -7973.57 \text{ V/m})$ per 1 V for the electrode used for the dc voltage application, where E_X, E_Y, E_Z are electric fields in the laboratory frame as shown in Fig. S1 (a). For the electrode used for the ac voltage application, $(E_X, E_Y, E_Z) = (13763.6 \text{ V/m}, -18844.1 \text{ V/m}, -1079.8 \text{ V/m})$ per 1 V. The electric fields in the NV frame, $E_x, E_y,$ and $E_z,$ are defined to be $E_x = E_Y \sin\theta - E_Z \cos\theta,$ and $E_y = E_X, E_z = -E_Y \cos\theta - E_Z \sin\theta,$ where $\sin\theta = \sqrt{1/3}$ and $\cos\theta = \sqrt{2/3}$ (Fig. S1 (b)(c)). Thus, $(E_x, E_y, E_z) = (-8571.3 \text{ V/m}, 12497.6 \text{ V/m}, 25932.3 \text{ V/m})$ per 1 V for the electrode used for the dc voltage application, and $(E_x, E_y, E_z) = (-9998.0 \text{ V/m}, 13763.6 \text{ V/m}, 16009.6 \text{ V/m})$ per 1 V for the electrode used for the ac voltage application. The applied ac voltage is estimated using the relation $V = \sqrt{PR},$ where V is the root-mean-square (RMS) voltage, P is the microwave power, R is the resistance. When 1 μW microwave is applied to the electrode at the end of the 50 Ω transmission line, $V = 7.1 \text{ mV}.$ Assuming the end of the electrode can be approximated to be an open circuit ($Z = \infty$), the voltage amplitude at the electrode is $7.1 \times \sqrt{2} \times 2 = 20 \text{ mV}.$ The factor $\sqrt{2}$ is introduced to convert the RMS voltage to the voltage amplitude. The factor 2 is required because the circuit is open at the end of the electrode.

-
- [1] J. R. Maze, A. Gali, E. Togan, Y. Chu, A. Trifonov, E. Kaxiras, and M. D. Lukin, *New Journal of Physics* **13**, 10.1088/1367-2630/13/2/025025 (2011), arXiv:1010.1338.

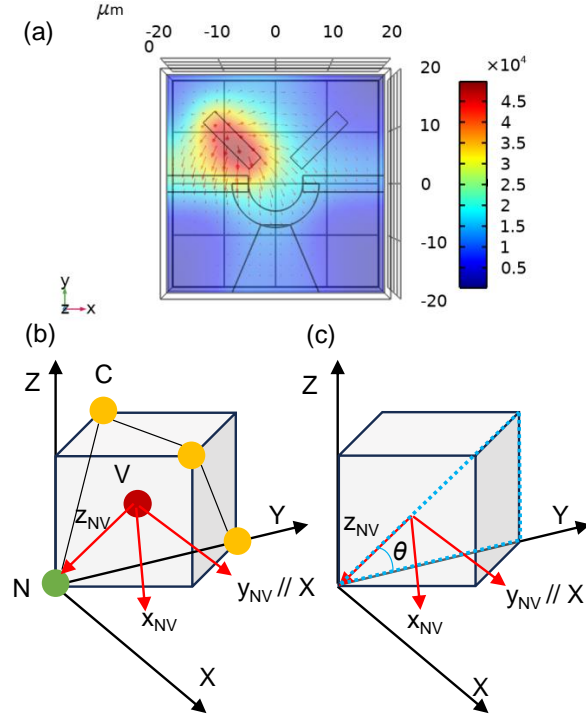


FIG. S1. (a) The electric field distribution around the electrode simulated by the FEM software. The applied voltage is 1 V. The unit of the color bar is V/m. (b) The relationship between the laboratory frame and the frame of NV center. C, N, and V correspond carbon atom, nitrogen atom, and vacancy, respectively. The direction of the NV center is estimated from the measurement of the optically-detected magnetic resonance. Only two of the four NV axes can be distinguished through the measurement. However, the distinction between the two types of axes only affects the sign of the electric field. Therefore, we define the NV axis as illustrated in the figure. z_{NV} is along the NV axis. x_{NV} and y_{NV} are defined following the definition of $|e_{x,y}\rangle$ in Ref. [1]. (c) We define θ as shown in the figure.